AIP Advances

Energy transport characteristics of converging Richtmyer–Meshkov instability

Cite as: AIP Advances **10**, 105302 (2020); https://doi.org/10.1063/5.0022280
Submitted: 03 September 2020 . Accepted: 10 September 2020 . Published Online: 01 October 2020

Yaowei Fu (符耀威), Changping Yu (于长平), and Xinliang Li (李新亮)

COLLECTIONS

Paper published as part of the special topic on Chemical Physics, Energy, Fluids and Plasmas, Materials Science and Mathematical Physics

View Online Export Citation CrossMark

ARTICLES YOU MAY BE INTERESTED IN

Turbulent mixing and transition criteria of flows induced by hydrodynamic instabilities
Physics of Plasmas **26**, 080901 (2019); https://doi.org/10.1063/1.5088745

Smoothed particle hydrodynamics simulation of converging Richtmyer–Meshkov instability
Physics of Fluids **32**, 086102 (2020); https://doi.org/10.1063/5.0015589

Effects of transverse shock waves on early evolution of multi-mode chevron interface
Physics of Fluids **32**, 106101 (2020); https://doi.org/10.1063/5.0023100

AIP Advances
Fluids and Plasmas Collection
READ NOW

AIP Publishing

© 2020 Author(s).

Energy transport characteristics of converging Richtmyer–Meshkov instability

Cite as: AIP Advances 10, 105302 (2020); doi: 10.1063/5.0022280
Submitted: 3 September 2020 • Accepted: 10 September 2020 •
Published Online: 1 October 2020

View Online Export Citation CrossMark

Yaowei Fu (符耀威),[1,2] Changping Yu (于长平),[1,2] and Xinliang Li (李新亮)[1,2,a)]

AFFILIATIONS

[1] LHD, Institute of Mechanics, Chinese Academy of Sciences, Beijing 100190, China
[2] School of Engineering Science, University of Chinese Academy of Sciences, Beijing 100049, China

[a)] Author to whom correspondence should be addressed: lixl@imech.ac.cn

ABSTRACT

In this paper, the Richtmyer–Meshkov (RM) instability in spherical and cylindrical converging geometries with a Mach number of about 1.5 is investigated by using the direct numerical simulation method. The heavy fluid is sulfur hexafluoride, and the light fluid is nitrogen. The shock wave converges from the heavy fluid into the light fluid. The main focus is on the energy transport characteristics in the mixing layer during the entire development process from early instability to late-time turbulent mixing. First, the turbulence kinetic energy transport equation is analyzed, and it is found that the production and dissipation mechanisms of the turbulence induced by the spherical and cylindrical converging RM instabilities in the mixing layer are the same. The turbulent diffusion terms are crucial in the whole development processes of the mixing layers. Before the reflected shock waves transit the interfaces, the dissipation terms can be ignored relative to other terms, and after that, the dissipation terms are close to the production terms and play an important role. The compressibility terms are approximate to the production terms and promote the production of turbulence kinetic energy in the later stage. The viscous diffusion terms can be ignored throughout the process. Then, the enstrophy transport equation is researched, and it is found that, in the mixing layers, the baroclinicity terms play a leading role in the early stage, while the vortex stretching terms play a leading role in the later stage, and the vortex stretching term of the spherical converging geometry develops faster than that of the cylindrical converging geometry. The compressibility terms are positive in the early stage, which promote the production of enstrophy. After the reflected shock waves transit the interfaces, the compressibility terms become negative, which inhibit the production of enstrophy. In addition, the results of the present direct numerical simulation also show that the density fluctuation spectra in the centers of the mixing layers of the spherical and cylindrical converging RM instabilities present the obvious −5/3 scaling law.

© 2020 Author(s). All article content, except where otherwise noted, is licensed under a Creative Commons Attribution (CC BY) license (http://creativecommons.org/licenses/by/4.0/). https://doi.org/10.1063/5.0022280

I. INTRODUCTION

When the shock wave interacts with the material interface with initial disturbance, because the direction of the pressure gradient and the direction of the density gradient are not collinear, $\nabla P \cdot \nabla \rho \neq 0$, baroclinic vorticity is deposited on the disturbed interface and induces the Richtmyer–Meshkov (RM) instability. The disturbance on the interface experiences linear and nonlinear growth and then leads to turbulent mixing. The RM instability is a very common flow phenomenon, which plays a very important role in the fields of inertial confinement fusion (ICF), supersonic combustion, and supernova explosion. For example, in ICF, the RM instability leads to turbulent mixing of fuel and ablative layer in the capsule, which further affects the compression of the capsule and the formation of the hot spot in the center and then results in ignition failure. In supersonic combustion, the shock wave passes through the interface of fuel and oxidant and accelerates the mixing of fuel and oxidant, which is beneficial to the combustion. In supernova explosion, when the shock wave caused by the outward projectile of matter converges toward the center and passes through the interface of different densities, the RM instability is induced and then affects the life evolution of stars.

Studies on the RM instability can date back to the 1950s. Markstein[1] first discovered this phenomenon. Richtmyer,[2] based on the analytical method of Rayleigh–Taylor (RT) instability,[3,4] was the first to conduct theoretical research on a sinusoidal single-mode

© Author(s) 2020

disturbed interface accelerated by a plane shock and put forward the impact model of disturbance growth. Later, Meshkov's[5] shock tube experiment result verified the accuracy of Richtmyer's theoretical model to some extent. Different from the RT instability, the RM instability occurs whether the shock wave is incident from heavy fluid into light fluid or from light fluid into heavy fluid. However, the development process of the interface disturbance is differs greatly in these two cases. If the shock wave is incident from a heavy fluid into a light fluid, the baroclinic vorticity deposited on the interface will first make the interface disturbance decrease gradually and then increase reversely. If the shock wave is incident from a light fluid into a heavy fluid, the baroclinic vorticity deposited on the interface will directly make the interface disturbance increase continuously.

Zhou[6,7] gave a detailed introduction to the research progress of plane RT and RM instabilities and a brief introduction to the flows with converging geometries in recent years. It can be seen that previous studies on the RM instability, whether experimental, theoretical, or numerical, have mostly focused on the relatively simple case of plane shock interacting with the disturbed interface. However, in nature or practical engineering applications, the RM instability is basically converging, such as the spherical converging shock wave–spherical interface or cylindrical converging shock wave–cylindrical interface. Compared with the plane case, the converging RM instability will be more complex due to the influences of the stronger compressibility, RT effect, and Bell–Plesset (BP) effect.

In terms of numerical research, Lombardini[8] used the large-eddy simulation (LES) method to study in detail the turbulent and mixing characteristics of the cylindrical converging RM instability in the turbulent mixing layer and compared these characteristics with the planar RM instability. Lombardini found that the turbulence was weakly compressible in the later mixing stage, and the inertial sub-region of the energy spectrum at the center of the cylindrical turbulent mixing layer presented a −5/3 scaling law, and the probability density function of the mixing fraction showed a weak bimodal characteristic. Then, Lombardini[9,10] introduced the spherical harmonic function disturbance and conducted LES on the spherical converging RM instability. It was found that, when the initial disturbance is a high wave number, the baroclinicity term played a major role, and the compressibility term had greater influence than the geometric converging effect. In the center of the turbulent mixing layer, the inertial sub-region of the kinetic energy and density spectrum also showed the −5/3 scaling law. Rafei[11] conducted three-dimensional high-resolution large-eddy simulations of turbulence mixing in spherical implosions with different initial perturbations. Wang *et al.*[12] carried out the numerical simulation of the spherical converging RM instability and found that there was strong anisotropy in the turbulent mixing layer, and energy was transported mainly in the radial direction. The radial velocity fluctuation energy spectrum presented an obvious −4/3 scaling law, and the velocity fluctuation energy spectra in the other two directions showed an obvious −1 scaling law. Zhai's[13] two-dimensional numerical simulation studied in detail the RT effect on the cylindrical converging RM instability. Mankbadi solved one-dimensional equations and studied the effects of viscosity and heat conduction on the spherical converging RM instability,[14] as well as the disturbance amplitude growth rate of the spherical converging RM instability with different initial pressure ratios and temperature ratios.[15]

In terms of experimental research, Hosseini[16] measured in detail the pressure evolution of the cylindrical converging RM instability during the shock wave implosion and reflection from the center. The influence of the BP effect on the growth of disturbance amplitude of the cylindrical converging RM instability was studied experimentally by Vandenboomgaerde's[17] shock tube experiment. Luo *et al.*[18–26] designed a semi-annular shock tube and conducted a lot of experiments on the cylindrical converging RM instability. By analyzing experimental data and taking into account the RT effect and compressibility effect, respectively, Luo *et al.* proposed two new disturbance amplitude growth models on the cylindrical converging RM instability based on the Bell model.

In terms of theoretical research, Mikaelian[27,28] analyzed the linear stability of the spherical and cylindrical converging RT and RM instability and derived the interface evolution equation. Based on the formal perturbation expansion and potential flow theory, Liu[29] proposed a simple method to study the influence of nonlinear effects on the development of the cylindrical converging RM instability. Later, starting from the Pade′ approximation and perturbation expansion directly on the perturbed interface, Liu[30] developed a nonlinear theory for the cylindrical converging RM instability under incompressible, inviscid, and irrotational assumptions, and obtained the fourth-order explicit solution in the weakly nonlinear region.

In previous studies, Schilling[31] and Thornber[32] have studied in detail the turbulence kinetic energy transport and mixing characteristics of planar RT and RM instabilities, respectively. In this paper, two direct numerical simulations for the spherical and cylindrical converging RM instabilities with a Mach number of about 1.5 are conducted using the high precision finite difference solver code, named as *OpenCFD − Comb*, developed by our group for the multicomponent flows. The heavy fluid is sulfur hexafluoride (SF6), the light fluid is nitrogen (N2), and the incident shock wave converges from the heavy fluid into the light fluid. The turbulence kinetic energy transport equation and enstrophy transport equation in the mixing layer of the spherical and cylindrical converging RM instabilities are analyzed and compared in detail.

II. COMPUTATIONAL SETUP

In the *OpenCFD − Comb* code, three-dimensional multicomponent Navier–Stokes (N–S) equations, including the mass conservation equation, momentum conservation equation, energy conservation equation, and component conservation equation, are discretely solved in the Cartesian coordinate system,

$$\begin{aligned}
&\frac{\partial \rho}{\partial t} + \frac{\partial(\rho u_i)}{\partial x_i} = 0,\\
&\frac{\partial(\rho u_i)}{\partial t} + \frac{\partial(\rho u_i u_j)}{\partial x_j} = -\frac{\partial P}{\partial x_i} + \frac{\partial \tau_{ij}}{\partial x_j},\\
&\frac{\partial E}{\partial t} + \frac{\partial[(E+P)u_j]}{\partial x_j} = \frac{\partial[u_i \tau_{ij} + q_j]}{\partial x_j},\\
&\frac{\partial \rho_k}{\partial t} + \frac{\partial(\rho_k u_i)}{\partial x_i} = \frac{\partial}{\partial x_i}\left[\rho D_{km} \frac{\partial Y_k}{\partial x_i}\right],
\end{aligned} \tag{1}$$

where ρ is the density of the mixture, $\rho_k = \rho Y_k$ is the density of species k, Y_k is the mass fraction of species k, u_i is the fluid

© Author(s) 2020

velocity in the i direction, P is the static pressure, $E = \rho(e + u_i u_i/2)$ is the total energy per unit volume, D_{km} is the mixture diffusion coefficient of species k, τ_{ij} is the viscous stress tensor, and q_j is the heat flux in the j direction,

$$\tau_{ij} = \mu\left(\frac{\partial u_i}{\partial x_j} + \frac{\partial u_j}{\partial x_i} - \frac{2}{3}\delta_{ij}\frac{\partial u_k}{\partial x_k}\right), \tag{2}$$

$$q_j = \lambda\frac{\partial T}{\partial x_j} + \rho\sum_{k=1}^{N} h_k D_{km}\frac{\partial Y_k}{\partial x_i}, \tag{3}$$

where μ is the viscosity coefficient of the mixture, λ is the heat conduction coefficient of the mixture, $h_k = C_{pk}T$ is the enthalpy of species k, and T is the temperature of the mixture. In this paper, it is assumed that each component is a calorically perfect gas with $\gamma_{N2} = 1.4$, $\gamma_{SF6} = 1.09$.

The viscosity and heat conduction coefficients of each species are calculated using the fitting polynomial method as in the *CHEMKIN*,[33]

$$\ln(\mu_k) = \sum_{n=1}^{N} b_{n,k}(\ln T)^{n-1}, \tag{4}$$

$$\ln(\lambda_k) = \sum_{n=1}^{N} c_{n,k}(\ln T)^{n-1}. \tag{5}$$

The viscosity coefficient and heat conductivity coefficient of the mixture are calculated by using the Wilke formula,[34]

$$\mu = \sum_{k=1}^{N}\frac{X_k\mu_k}{\sum_{j=1}^{N} X_j\phi_{kj}}, \tag{6}$$

$$\phi_{kj} = \frac{1}{\sqrt{8}}\left(1 + \frac{W_k}{W_j}\right)^{-1/2}\left[1 + \left(\frac{W_j}{W_k}\right)^{1/4}\left(\frac{\mu_k}{\mu_j}\right)^{1/4}\right]^2, \tag{7}$$

$$\lambda = \frac{1}{2}\left(\sum_{k=1}^{N} X_k\lambda_k + \frac{1}{\sum_{k=1}^{N} X_k\lambda_k}\right), \tag{8}$$

where W_k is the molecular weight of species k and X_k is the volume fraction of species k and is defined as

$$X_k = \frac{Y_k\overline{W}}{W_k}, \tag{9}$$

$$\overline{W} = \sum_{k=1}^{N} X_k W_k = \frac{1}{\sum_{k=1}^{N} Y_k/W_k}. \tag{10}$$

The mixture diffusion coefficient of species k is calculated using the Schmidt number $Sc_k = \mu/\rho D_{km}$. The Schmidt numbers of SF6 and N2 are both assigned the value of 1. The sixth-order monotonicity-preserving optimized scheme (OMP6)[35] is employed to discretize the convective terms, and the eighth-order central difference scheme is adopted for the viscous terms. The third-order Runge–Kutta approach is used for the time advancement.

The initial conditions of a flow field have a significant impact on flows induced by RT and RM instabilities. A detailed description about the initial conditions can be found in the paper of Zhou.[36] In the present paper, the spherical harmonic function, same as that of Lombardini, is used to generate the initial perturbed interface,

$$\begin{aligned}
\psi(r,\theta,\varphi) &= \frac{1}{2}\left\{1 - \tanh\left[\frac{r - \xi_0(\theta,\varphi)}{L_r}\right]\right\},\\
\xi_0(\theta,\varphi) &= R_0 - a_0|f(R_0,\theta,\varphi)|,\\
f(R_0,\theta,\varphi) &= \sum_{l=0}^{M}\sum_{m=-l}^{l} f_{lm}Y_{lm}(\theta,\varphi),\\
f_{lm} &= \sqrt{(2l+1)C_l}\frac{\cos(2\pi\omega_l^m)}{\sqrt{\sum_{i=-l}^{l}\cos\left(2\pi\omega_l^i\right)}},\\
C_l &= \frac{1}{4(2l_0+1)}\frac{1}{\sigma_0\sqrt{2\pi}}\exp\left[-\frac{(l-l_0)^2}{2\sigma_0{}^2}\right].
\end{aligned} \tag{11}$$

Here, ω_l^m is the random number between 0 and 1, which is the same for all direct numerical simulations in this paper. The radial distribution of the mass fraction of the light fluid is $Y_{N2} = \psi$. For the spherical converging RM instability, $r = \sqrt{x^2+y^2+z^2}, \varphi = a\tan 2(z,x), \theta = a\tan 2(\sqrt{x^2+z^2}, y)$. For the cylindrical converging RM instability, $r = \sqrt{x^2+y^2}, \varphi = a\tan 2(y,x), \theta = \pi(k-1)/(n_k - 1)$, where n_k is the grid number in the k direction. In addition, $R_0 = 7$ mm, $a_0 = 0.375$ mm, $L_r = 0.2$ mm, $M = 40$, $l_0 = 20$, $\sigma_0 = l_0/15$. The position of the shock wave at the initial time is located at $R_{sp} = 8.5$ mm. The main computation domains for the present spherical and cylindrical converging RM instabilities in the Cartesian coordinate system are $L_x = L_y = L_z = L = 20$ mm. In order to avoid the influence of the boundary, a nonuniform coarse grid sponge layer with a length of $40L$ is added at each nonperiodic boundary. It is worth noting that only the spanwise direction of the cylindrical converging RM instability is periodic. Table I records the flow field parameters at the initial time, and Fig. 1 is a schematic of the two-dimensional middle section at the initial time. The shock and interface positions are marked in Fig. 1.

In order to verify the mesh convergence, three sets of meshes are designed for the cylindrical converging RM instability. The total structured node number in the main computation domain is 512^3, 768^3, and 1024^3, respectively. In the subsequent processing of the data, the spherical or cylindrical shell averaging method is used. When processing data in the following paper, unless otherwise specified, the density of light fluid ρ_l, radial velocity after the shock wave U_r, and radius of light fluid R_0 at the initial time are used to

TABLE I. Flow parameters at the initial time, where U_r is the radial velocity.

	Pre-shock		Post-shock
	N2	SF6	SF6
P (Pa)	101 325	101 325	233 435.425
ρ (kg/m^3)	1.145	5.971	12.748
U_r (m/s)	0	0	108.456

© Author(s) 2020

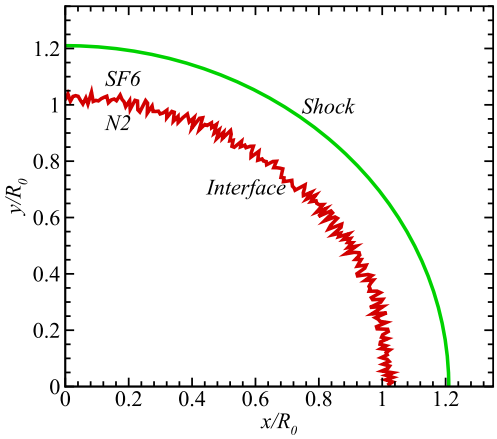

FIG. 1. Schematic of the two-dimensional middle section at the initial time.

normalize the present numerical results. Figure 2(a) describes the temporal variations of inner and outer radii of the cylindrical converging RM instability, where the inner radius, denoted by r_1, is the position of $Y_{SF6} = 0.01$ and the outer radius, denoted by r_2, is the position of $Y_{N2} = 0.01$. It can be found that the inner and outer radii of the three sets of meshes are almost identical. Figures 2(b)–2(d), respectively, show the radial distributions of densities, turbulence kinetic energy [see Eq. (12)], and density-weighted root mean square of radial velocities at the final time, i.e., $t = 0.2$ ms. It can be seen that the results of the three sets of meshes have some slight differences near the convergence center due to the fewer grid points of shell averaging, and the results of other positions are also almost identical. In order to ensure the reliability of our direct numerical simulation (DNS), the results on the mesh of 1024^3 is selected for subsequent analysis of the cylindrical converging RM instability, and the same mesh is used directly for DNS of the spherical converging RM instability.

III. RESULTS AND DISCUSSIONS

The isosurfaces of the light fluid mass fraction $Y_{N2} = 0.1$ for the spherical and cylindrical converging RM instabilities at different times are displayed, respectively, in Figs. 3 and 4. By comparing these isosurfaces, it can be found that the development processes of interface disturbances of the spherical and cylindrical converging RM instabilities are basically the same. First of all, because the shock waves are incident from heavy fluid into light fluid, the amplitudes of interface disturbances are first flattened by the incident shock waves after the first transmission of the shock waves at $t = 0.01$ ms and then increase in reverse, resulting in the so-called phase inversion. In this process, the flow fields are dominated by large-scale bubbles. Subsequently, after the reflected shock waves pass through the material interfaces at $t = 0.04$ ms, large-scale bubbles are quickly broken by

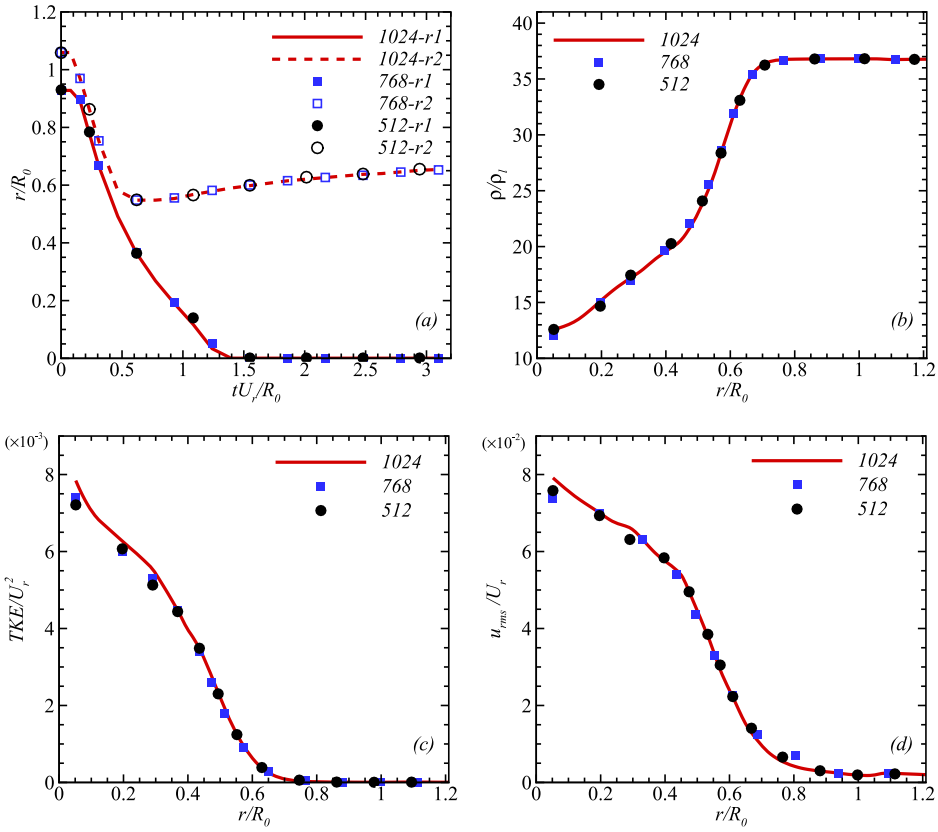

FIG. 2. Mesh convergence verification of the cylindrical converging RM instability: (a) temporal variation of inner and outer radii; (b) distribution of density at $t = 0.2$ ms; (c) distribution of turbulence kinetic energy at $t = 0.2$ ms; and (d) distribution of density-weighted root mean square of radial velocity at $t = 0.2$ ms.

© Author(s) 2020

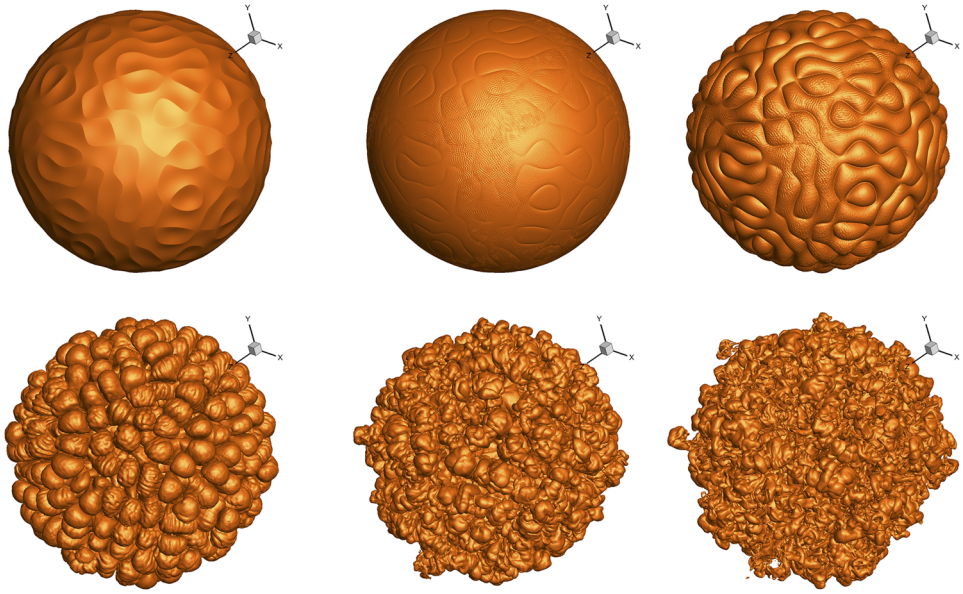

FIG. 3. Isosurfaces of Y_{N2} = 0.1 for the spherical converging RM instability at t = 0 ms, 0.01 ms, 0.02 ms, 0.04 ms, 0.08 ms, and 0.2 ms.

the reflected shock waves, and the flow fields are dominated by the small-scale structures. Figures 5 and 6, respectively, show the density fields on the middle sections of the three directions in the Cartesian coordinate system for the spherical and cylindrical converging RM instabilities at t = 0.2 ms. It can be seen that, at the final time of simulation, the small-scale structures of the flow fields are particularly abundant, and the light/heavy fluids enter the stage of turbulent mixing.

Figure 7(a) describes the temporal variation processes of the main shock wave positions for the spherical and cylindrical converging RM instabilities, in which the shock wave positions are identified by the absolute maximum of velocity divergence $\nabla \cdot \mathrm{V}$. On the whole, the main shock waves travel uniformly with different velocities in different materials. Before the main shock waves hit the material interfaces for the first time, the spherical and cylindrical converging shock waves move at the same speed. However, after that, the spherical converging/reflected shock wave moves significantly faster than the cylindrical converging/reflected shock wave.

The mixing width is one of the most important physical quantities in practical engineering applications. For RT and RM instabilities, there are several different definitions to describe the mixing.[37,38] The most common definition for numerical simulations of miscible fluid is the threshold mixing width. Figure 7(b) shows the

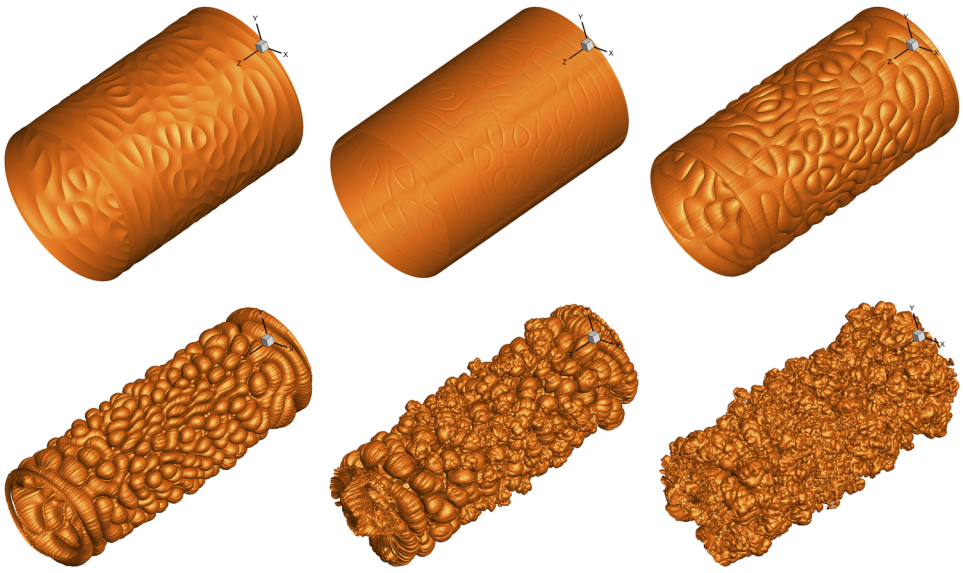

FIG. 4. Isosurfaces of Y_{N2} = 0.1 for the cylindrical converging RM instability at t = 0 ms, 0.01 ms, 0.02 ms, 0.04 ms, 0.08 ms, and 0.2 ms.

© Author(s) 2020

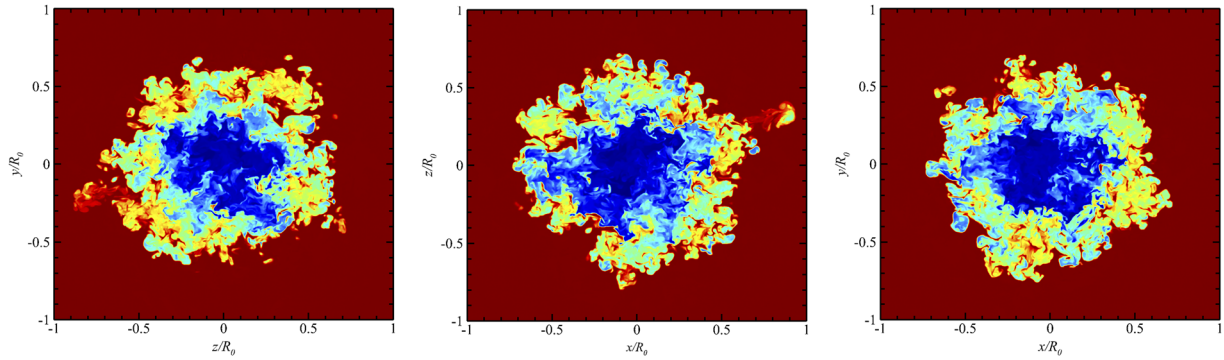

FIG. 5. Density fields on middle sections for the spherical converging RM instability at t = 0.2 ms.

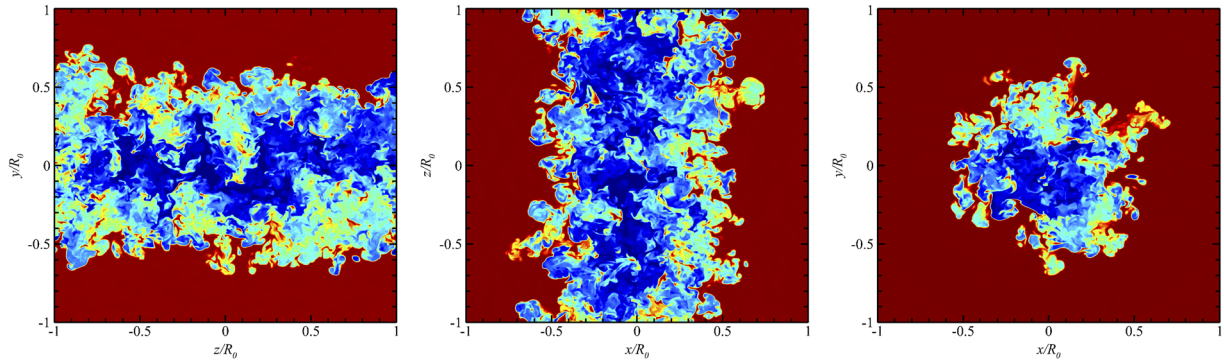

FIG. 6. Density fields on the middle sections for the cylindrical converging RM instability at t = 0.2 ms.

temporal variations of inner radii, outer radii, and the widths of mixing layers for the spherical and cylindrical converging RM instabilities. The widths of mixing layers are defined as $h = r_2 - r_1$. It can be found from Fig. 7(b) that the widths of the mixing layers for the spherical and cylindrical converging RM instabilities have both reached asymptotic saturation, and the widths of the mixing layers of the spherical converging RM instability are significantly larger than those of the cylindrical converging RM instability. The development

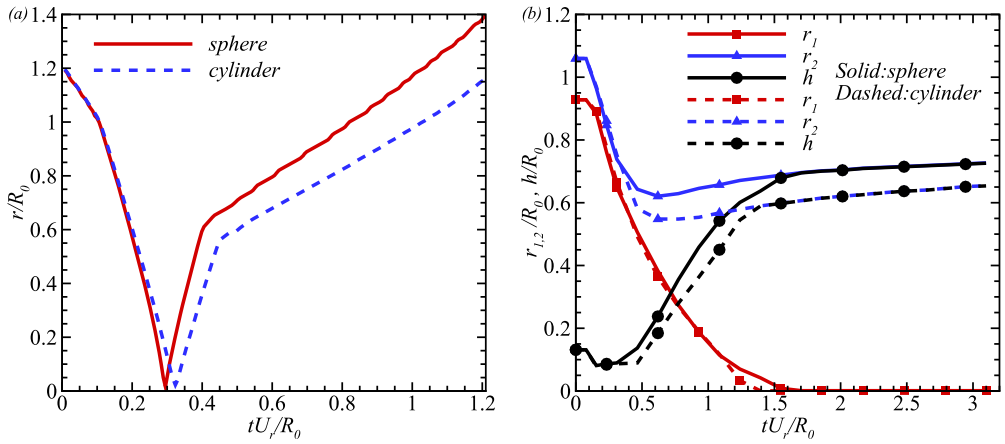

FIG. 7. (a) Temporal variations of shock wave positions. (b) Temporal variations of the spherical/cylindrical inner and outer radii and the widths of mixing layers.

© Author(s) 2020

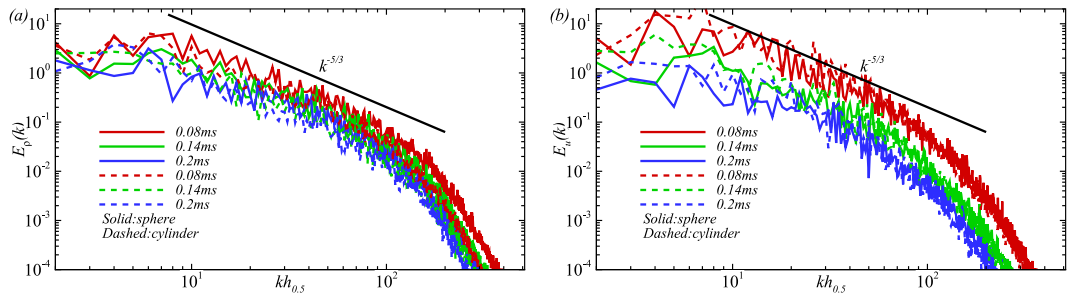

FIG. 8. Density (a) and radial velocity (b) fluctuation spectra of the spherical/cylindrical converging RM instability in the centers of mixing layers at different times.

of inner radii is basically the same, but the outer radii differ greatly. The main reason is that the cylindrical interface is more severely compressed by the incident shock wave than the spherical interface under the same incident shock wave Mach number. Because the spherical interface converges from three directions to the center point, and the cylindrical interface converges from two directions to the centerline, the pressure and light fluid density in the spherical interface are greater than those in the cylindrical interface, which restrains the outer radius of the spherical interface from converging to the center point.

Figure 8 displays the density and radial velocity fluctuation spectra of the spherical and cylindrical converging RM instabilities

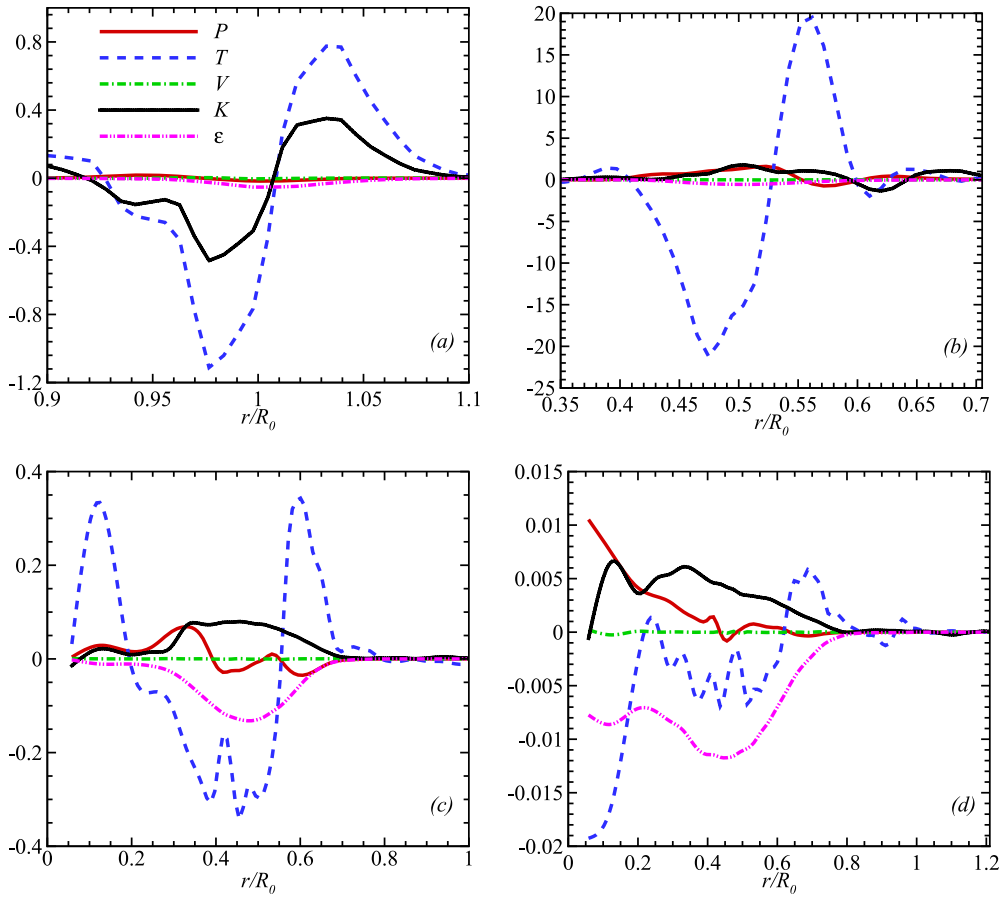

FIG. 9. Turbulence kinetic energy transport equation in the mixing layer of the spherical converging RM instability: (a) t = 0.01 ms, (b) t = 0.04 ms, (c) t = 0.08 ms, and (d) t = 0.2 ms.

© Author(s) 2020

in the centers of mixing layers at different times. Here, the centers of mixing layers are the position of $h_{0.5} = (r_1 + r_2)/2$. It can be seen that the density and radial velocity fluctuation spectra of the spherical and cylindrical converging RM instabilities are basically overlapped by using the $h_{0.5}$ to normalize the wave numbers at any given moment. In addition, the inertial sub-region of density spectra for spherical and cylindrical converging RM instabilities in the centers of mixing layers present an obvious −5/3 scaling law all the time, which is the same as the result of Lombardini. However, the −5/3 scaling law of the inertial sub-region of radial velocity fluctuation spectra is narrow. With the turbulence decaying, the inertial sub-region of radial velocity fluctuation spectra becomes less and less obvious.

Turbulent mixing induced by the converging RM instability in the mixing layer plays a very important role in ICF. Therefore, the analysis of the turbulence kinetic energy budget is helpful to deepen the understanding of the converging RM instability and to build a new turbulence model or improve existing turbulence models. The turbulence kinetic energy k and its transport equation can be derived from the compressible N–S equations (1),

$$k = \frac{1}{2}\langle u_i'' u_i'' \rangle, \tag{12}$$

$$\frac{\partial \overline{\rho} k}{\partial t} + \frac{\partial \overline{\rho} k \langle u_j \rangle}{\partial x_j} = -\frac{\partial}{\partial x_j}\left[\frac{1}{2}\overline{\rho}\langle u_i'' u_i'' u_j'' \rangle + \overline{P' u_j''}\right] + \frac{\partial}{\partial x_j}\left[\overline{u_i'' \tau_{ji}''}\right] - \overline{\rho}\langle u_i'' u_j'' \rangle \frac{\partial \langle u_i \rangle}{\partial x_j} - \overline{\tau_{ji}'' \frac{\partial u_i''}{\partial x_j}} + \left[\overline{P' \frac{\partial u_i''}{\partial x_i}} - \overline{u_j''} \frac{\partial P}{\partial x_j} + \overline{u_i''} \frac{\partial \langle \tau_{ji} \rangle}{\partial x_j}\right]. \tag{13}$$

Here, for any variable f, an overbar denotes the Reynolds averaging, and

$$\langle f \rangle = \overline{\rho f}/\overline{\rho}, \tag{14}$$

$$f'' = f - \langle f \rangle, \tag{15}$$

$$f' = f - \overline{f}. \tag{16}$$

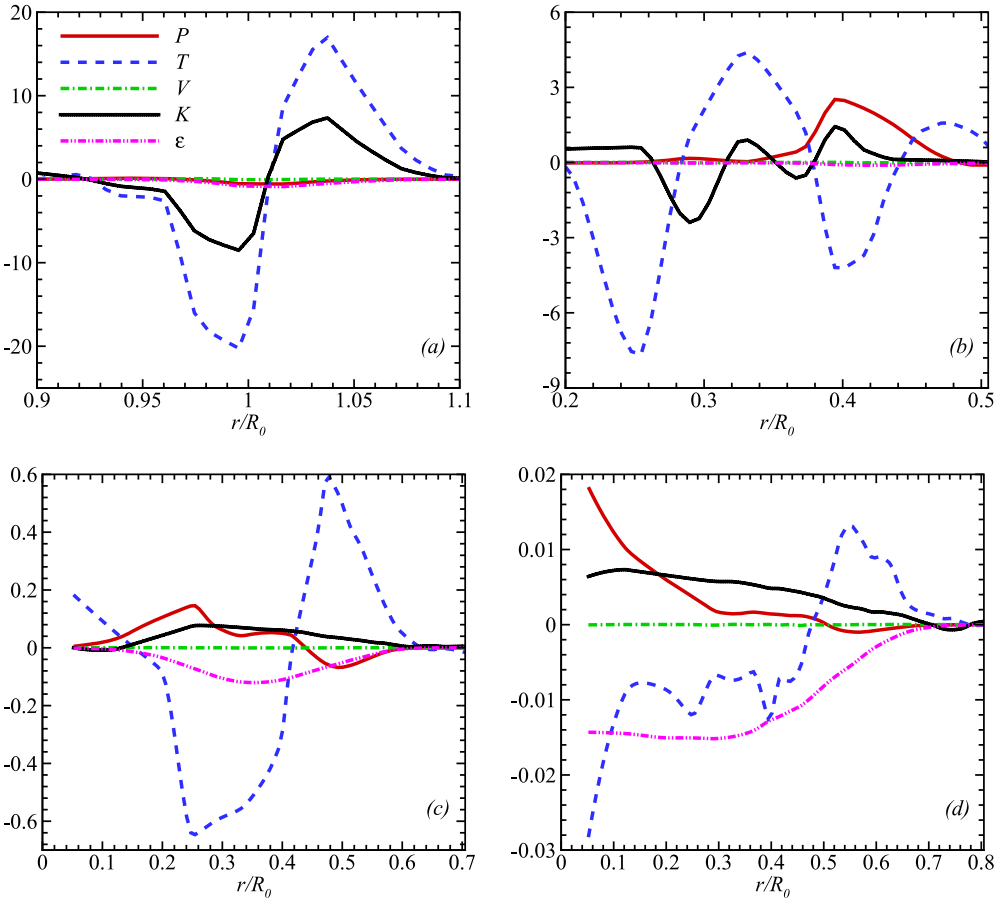

FIG. 10. Turbulence kinetic energy transport equation in the mixing layer of the cylindrical converging RM instability: (a) t = 0.01 ms, (b) t = 0.04 ms, (c) t = 0.08 ms, and (d) t = 0.2 ms.

© Author(s) 2020

On the right-hand side of the turbulence kinetic energy transport equation (13), the first term is the turbulent diffusion term T, reflecting the transport of turbulent kinetic energy due to the turbulence effect. The second term is the viscous diffusion term V, reflecting the turbulent kinetic energy diffusion due to molecular viscosity. The third term is the production term P, reflecting the conversion of average energy to turbulence kinetic energy. The fourth term is the dissipation term ε, reflecting the dissipation of turbulence kinetic energy into internal energy. The last term is the compressible term K, reflecting the change in turbulence kinetic energy due to compressibility.

Figures 9 and 10 show the radial distributions of all the terms of the turbulence kinetic energy transport equation in the mixing layer of the spherical and cylindrical converging RM instabilities at different times, respectively. By comparing the two figures, it can be found that the turbulent diffusion term T has a very important effect on the development of the mixing layer. Before the mixing layer reaches the converging center, in the mixing layer, the turbulent diffusion term T is negative in the middle position and positive on both sides, which indicates that the turbulence kinetic energy diffuses from the mixing layer to both sides. After that, the turbulence kinetic energy diffuses slowly to the outer boundary. In the whole development process of the mixing layer, the viscous diffusion term V can be ignored relative to other terms. The dissipation term ε is negligible before reshock. However, at the later stage, it is close to the production term P and plays an important role. The compressible term K is close to the production term P and is non-negligible at the later stage of turbulent mixing, which means that, similar to Lombardini's conclusion, the turbulent mixing layer is compressible in the later stage. In addition, the compressible term K mainly regulates the radial distribution of turbulence kinetic energy in the early stage and promotes the production of turbulence kinetic energy in the later stage. In general, the trends of the turbulence kinetic energy transport equations for the spherical and cylindrical converging RM instabilities are basically the same in the whole development process of the turbulent mixing layer, which indicates that the generation mechanism of the turbulence for the mixing layer of the spherical and cylindrical converging RM instabilities is the same. The main mechanisms of turbulence decaying in the later stage of the mixing layer are turbulent diffusion and dissipation.

It is well known that the RM instability is mainly caused by baroclinic vorticity, so the analysis of the equations related to vortex dynamics can reveal the intrinsic mechanism of the spherical and cylindrical RM instabilities more clearly and directly. Consider the

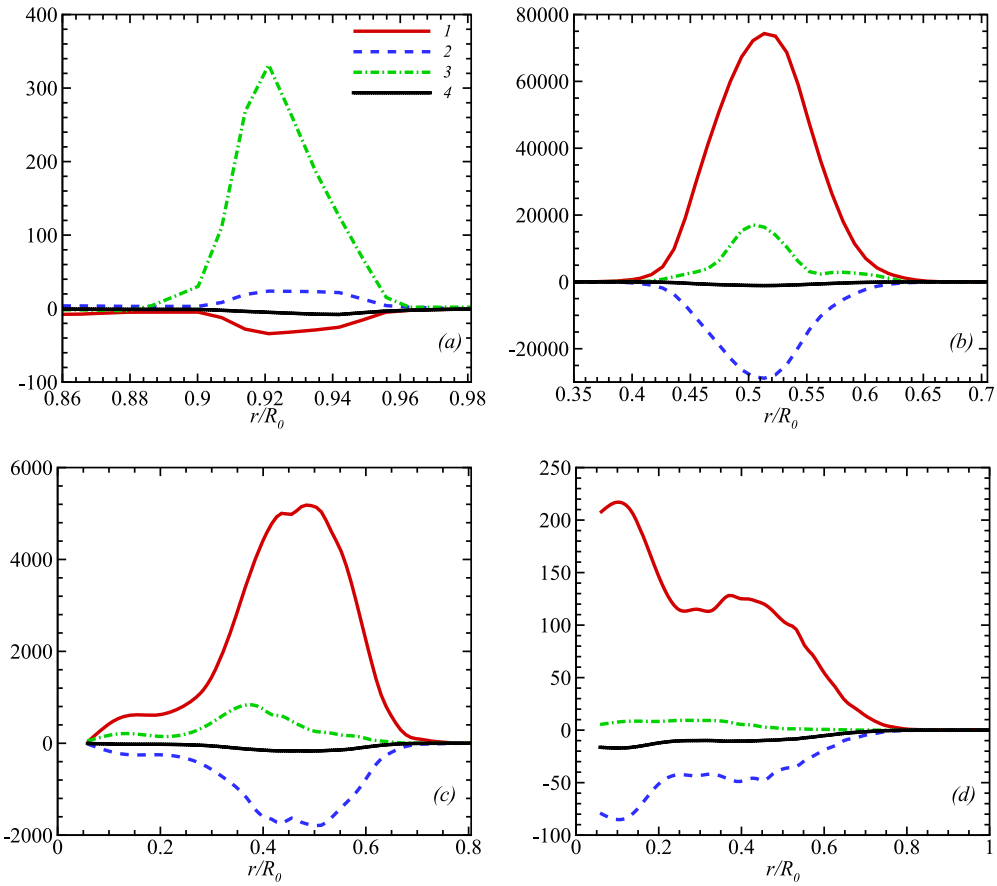

FIG. 11. Enstrophy transport equation in the mixing layer of the spherical converging RM instability: (a) t = 0.01 ms, (b) t = 0.04 ms, (c) t = 0.08 ms, and (d) t = 0.2 ms.

© Author(s) 2020

vortex dynamics equation

$$\frac{d\vec{\omega}}{dt} = \vec{\omega}\cdot\nabla\vec{V} - \vec{\omega}\left(\nabla\cdot\vec{V}\right) - \nabla\cdot\left(\frac{1}{\rho}\right)\times\nabla P + \lambda\nabla^2\vec{\omega}. \quad (17)$$

Enstrophy is defined as follows:

$$\Omega = \frac{1}{2}\vec{\omega}\cdot\vec{\omega}. \quad (18)$$

The enstrophy can be understood as the quantity directly related to the kinetic energy in the flow model that corresponds to dissipation effects in the fluid. It is particularly important in the study of turbulent flows. The enstrophy transport equation can be derived from the vortex dynamics equation (17),

$$\frac{d\Omega}{dt} = \vec{\omega}\cdot\left(\vec{\omega}\cdot\nabla\vec{V}\right) - \vec{\omega}\cdot\left[\vec{\omega}\left(\nabla\cdot\vec{V}\right)\right] - \vec{\omega}\cdot\left[\nabla\cdot\left(\frac{1}{\rho}\right)\times\nabla P\right] + \vec{\omega}\cdot\left(\lambda\nabla^2\vec{\omega}\right). \quad (19)$$

Referring to the definition of the right-hand side terms of the vortex dynamics equation (17), it is still defined here that the first term at the right-hand side of Eq. (19) is the vortex stretching term, the second term is the compressibility term, the third term is the baroclinicity term, and the fourth term is the viscous dissipation term.

Figures 11 and 12 show the radial distributions of all terms of the enstrophy transport equation in the mixing layers of the spherical and cylindrical converging RM instabilities at different times, respectively. By comparing Figs. 11 and 12, it can been found that the viscous dissipation terms can be ignored compared with other terms in the whole development processes of the mixing layers for the spherical and cylindrical converging RM instabilities. The baroclinicity terms play a leading role in the early stage, while the vortex stretching terms play a leading role in the later stage. Moreover, the vortex stretching terms of the spherical converging RM instability develop faster than those of the cylindrical converging RM instability. When the reflected shock waves pass through the interfaces, i.e., t = 0.04 ms, the vortex stretching term of the spherical converging RM instability has been far larger than the baroclinicity term. However, at this moment in time, the baroclinicity term of the cylindrical converging RM instability is still much larger than other term. The compressibility terms are positive in the early stage, which promote the production of enstrophy. After the reflected shock waves pass through the interfaces,

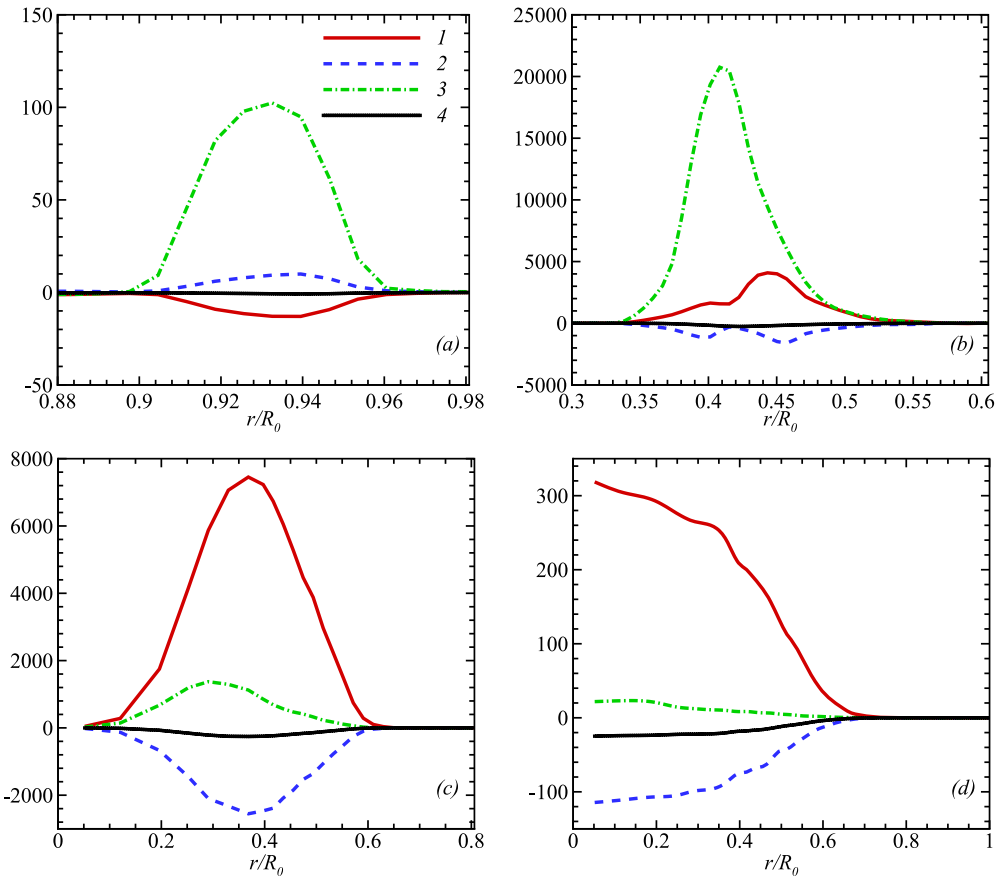

FIG. 12. Enstrophy transport equation in the mixing layer of the cylindrical converging RM instability: (a) t = 0.01 ms, (b) t = 0.04 ms, (c) t = 0.08 ms, and (d) t = 0.2 ms.

© Author(s) 2020

the compressibility terms become negative and the enstrophy is suppressed.

IV. CONCLUSIONS

In this paper, the converging RM instability at the spherical shock wave–spherical interface and cylindrical shock wave–cylindrical interface is studied by means of the direct numerical simulation method, and the turbulence kinetic energy transport equation and enstrophy transport equation in the entire development process of the RM mixing layer are analyzed. First of all, our numerical results show that the density fluctuation spectra in the centers of the spherical and cylindrical converging RM instability mixing layers present the obvious −5/3 scaling law. Then, the converging shock waves compress the cylindrical interface more seriously than the spherical interface. In addition, the analysis of the turbulence kinetic energy transport equation shows that the mechanisms of turbulent production and dissipation in the mixing layers of the spherical and cylindrical converging RM instabilities are the same, and the turbulent diffusion and dissipation are the main mechanisms of turbulence decaying in the later stage. The analysis of the enstrophy transport equation shows that, in the early stage of the developments of the spherical and cylindrical converging RM instability mixing layers, the baroclinicity terms play a leading role, but after the reflected shock waves pass through the interfaces, the vortex stretching terms gradually exceed the baroclinicity terms and play a leading role. Moreover, the vorticity stretching term of the spherical converging RM instability develops faster than the cylindrical converging RM instability.

ACKNOWLEDGMENTS

This work was supported by the National Key Research and Development Program of China (Grant Nos. 2016YFA0401200, 2019YFA0405300), NSFC Projects (Grant No. 91852203), the Science Challenge Project (Grant No. TZ2016001), and the Strategic Priority Research Program of Chinese Academy of Sciences (Grant Nos. XDA17030100 and XDC01000000). The authors thank the National Supercomputer Center in Tianjin (NSCC-TJ) and the National Supercomputer Center in GuangZhou (NSCC-GZ) for providing computer time.

DATA AVAILABILITY

The data that support the findings of this study are available from the corresponding author upon reasonable request.

REFERENCES

[1]G. H. Markstein, "Flow disturbances induced near a slightly wavy contact surface, or flame front, traversed by a shock wave," J. Aerosp. Sci. **24**, 238–239 (1957).
[2]R. D. Richtmyer, "Taylor instability in shock acceleration of compressible fluids," Commun. Pure Appl. Math. **13**, 297–319 (1960).
[3]Lord Rayleigh, "Investigation of the character of the equilibrium of an incompressible heavy fluid of variable density," Sci. Pap. **s1-14**, 170–177 (1882).
[4]G. L. Taylor, "The instability of liquid surfaces when accelerated in a direction perpendicular to their planes. I," Proc. R. Soc. London, Ser. A **201**, 192–196 (1950).
[5]E. E. Meshkov, "Instability of the interface of two gases accelerated by a shock wave," Fluid Dyn. **4**, 101–104 (1969).
[6]Y. Zhou, "Rayleigh–Taylor and Richtmyer–Meshkov instability induced flow, turbulence, and mixing. I," Phys. Rep. **720-722**, 1–136 (2017).
[7]Y. Zhou, "Rayleigh–Taylor and Richtmyer–Meshkov instability induced flow, turbulence, and mixing. II," Phys. Rep. **723-725**, 1–160 (2017).
[8]M. Lombardini, "Richtmyer–Meshkov instability in converging geometries," Ph.D. thesis, California Institute of Technology, 2008.
[9]M. Lombardini, "Turbulent mixing driven by spherical implosions. Part 1. Flow description and mixing-layer growth," J. Fluid Mech. **748**, 85–112 (2014).
[10]M. Lombardini, "Turbulent mixing driven by spherical implosions. Part 2. Turbulence statistics," J. Fluid Mech. **748**, 113–142 (2014).
[11]M. Rafei, "Three-dimensional simulations of turbulent mixing in spherical implosions," Phys. Fluids **31**, 114101 (2019).
[12]T. Wang, "Numerical investigations of interface instability and turbulent mixing driven by implosion," Sci. Sin.-Phys. Mech. Astron. **50**, 104704 (2020).
[13]Z. Zhai, "Numerical study on Rayleigh–Taylor effect on cylindrically converging Richtmyer–Meshkov instability," Sci. China-Phys. Mech. Astron. **62**, 124712 (2019).
[14]M. R. Mankbadi, "Viscous effects on the non-classical Rayleigh–Taylor instability of spherical material interfaces," Shock Waves **23**, 603–617 (2013).
[15]M. R. Mankbadi, "Compressible inviscid instability of rapidly expanding spherical material interfaces," Phys. Fluids **24**, 034106 (2012).
[16]S. H. R. Hosseini, "Experimental study of Richtmyer–Meshkov instability induced by cylindrical shock waves," Phys. Fluids **17**, 084101 (2005).
[17]M. Vandenboomgaerde, "Nonlinear growth of the converging Richtmyer–Meshkov instability in a conventional shock tube," Phys. Rev. Fluids **3**, 014001 (2018).
[18]F. Lei, "Nonlinear growth of the converging Richtmyer–Meshkov instability in a conventional shock tube," J. Fluid Mech. **826**, 819–829 (2017).
[19]X. Luo, "A semi-annular shock tube for studying cylindrically converging Richtmyer–Meshkov instability," Phys. Fluids **27**, 091702 (2015).
[20]Z. Zhai, "Refraction of cylindrical converging shock wave at an air/helium gaseous interface," Phys. Fluids **29**, 016102 (2017).
[21]J. Ding, "Measurement of a Richtmyer–Meshkov instability at an air-SF_6 interface in a semiannular shock tube," Phys. Rev. Lett. **119**, 014501 (2017).
[22]Y. Liang, "Interaction of strong converging shock wave with SF_6 gas bubble," Sci. China-Phys. Mech. Astron. **61**, 064711 (2018).
[23]X. Luo, "Long-term effect of Rayleigh–Taylor stabilization on converging Richtmyer–Meshkov instability," J. Fluid Mech. **849**, 231–244 (2018).
[24]X. Luo, "Nonlinear behaviour of convergent Richtmyer–Meshkov instability," J. Fluid Mech. **877**, 130–141 (2019).
[25]J. Ding, "Convergent Richtmyer–Meshkov instability of a heavy gas layer with perturbed outer interface," J. Fluid Mech. **878**, 277–291 (2019).
[26]D. Ma, "Study on Richtmyer–Meshkov instability at heavy/light single-mode interface," Sci. Sin.-Phys. Mech. Astron. **50**, 104705 (2020).
[27]K. O. Mikaelian, "Rayleigh–Taylor and Richtmyer–Meshkov instabilities and mixing in stratified spherical shells," Phys. Rev. A **42**, 3400–3420 (1990).
[28]K. O. Mikaelian, "Rayleigh–Taylor and Richtmyer–Meshkov instabilities and mixing in stratified cylindrical shells," Phys. Fluids **17**, 094105 (2005).
[29]W. Liu, "Cylindrical effects on Richtmyer–Meshkov instability for arbitrary Atwood numbers in weakly nonlinear regime," Phys. Fluids **19**, 072108 (2012).
[30]W. Liu, "Nonlinear theory of classical cylindrical Richtmyer–Meshkov instability for arbitrary Atwood numbers," Phys. Fluids **21**, 062119 (2014).
[31]O. Schilling, "Analysis of turbulent transport and mixing in transitional Rayleigh–Taylor unstable flow using direct numerical simulation data," Phys. Fluids **22**, 105102 (2010).
[32]B. Thornber, "Turbulent transport and mixing in the multimode narrowband Richtmyer–Meshkov instability," Phys. Fluids **31**, 096105 (2019).
[33]R. Design, CHEMKIN/CHEMKIN-PRO Theory Manual, 2008.

© Author(s) 2020

[34]C. R. Wilke, "A viscosity equation for gas mixtures," J. Chem. Phys. **18**, 517–519 (1950).
[35]X. Li, "Optimized sixth-order monotonicity-preserving scheme by nonlinear spectral analysis," Int. J. Numer. Methods Fluids **73**, 560–577 (2013).
[36]Y. Zhou, "Turbulent mixing and transition criteria of flows induced by hydrodynamic instabilities," Phys. Plasmas **26**, 080901 (2019).
[37]Y. Zhou, "Time-dependent study of anisotropy in Rayleigh–Taylor instability induced turbulent flows with a variety of density ratio," Phys. Fluids **31**, 084106 (2019).
[38]Y. Zhou, "Asymptotic behavior of the mixed mass in Rayleigh–Taylor and Richtmyer–Meshkov instability induced flows," Phys. Plasmas **23**, 052712 (2016).

© Author(s) 2020